The multi-field coupled vibration analysis of AT-cut quartz crystal resonators with parallelism error

Mengjie Li[1], Nian Li[1, 2], Peng Li[1, 2], Dianzi Liu[3], Iren E Kuznetsova[4], Zhenghua Qian[1, 2*] and Tingfeng Ma[5]

[1]*State Key Laboratory of Mechanics and Control of Mechanical Structures, College of Aerospace Engineering, Nanjing University of Aeronautics and Astronautics, Nanjing China;* [2]*Nanjing University of Aeronautics and Astronautics Shenzhen Research Institute, Shenzhen, China;* [3]*School of Engineering, University of East Anglia, Norwich NR4 7TJ, U.K.;* [4]*Kotel'nikov Institute of Radio Engineering and Electronics of RAS, Moscow, Russia;* [5]*Key Laboratory of Impact and Safety Engineering, Ministry of Education, Ningbo University, Ningbo China*

*Corresponding author, E-mail: qianzh@nuaa.edu.cn.

Abstract During the fabrication of quartz crystal resonators (QCRs), parallelism error is inevitably generated, which is rarely investigated. In order to reveal the influence of parallelism error on the working performance of QCRs, the coupled vibration of a non-paralleled AT-cut quartz crystal plate with electrodes is systematically studied from the views of theoretical analysis and numerical simulations. The two-dimensional thermal incremental field equations are solved for the free vibration analysis via the coefficient-formed partial differential equation (PDE) module of the COMSOL Multiphysics software, from which the frequency spectra, frequency-temperature curves, and mode shapes are discussed in detail. Additionally, the piezoelectric module is utilized to obtain the admittance response under different conditions. It is demonstrated that the parallelism error reduces the resonant frequency. Additionally, symmetry broken by the non-parallelism increases the probability of activity dip and is harmful to QCR's thermal stability. However, if the top and bottom surfaces incline synchronously in the same direction, the influence of parallelism error is tiny. The conclusions achieved are helpful for the QCR design, and the present methodology can also be used for other wave devices.

Keywords: Quartz crystal resonators; parallelism error; resonant frequency; mode coupling; admittance.

1. Introduction

As a key component of narrow-band filters, the quartz crystal resonator (QCR) consisting of a quartz crystal plate with electrodes on one or both surfaces, is widely used to generate oscillation frequency for communications [1-3]. Due to the piezoelectricity of quartz, the voltage imposed on the electrodes can be transformed into plate vibration with a fixed working frequency. Owing to some unique superiorities, *e.g.*, high frequency, small size, excellent stability, and easily embedded with chips, QCR has been widely

utilized in electronic products [4,5].

Generally speaking, the fundamental thickness-shear (TSh) mode with its resonant frequency mainly determined by the reciprocal of plate thickness is the working mode of QCR. It is expected that a pure TSh mode can be excited, so that the plate vibration can keep stable to some extent. However, because of the anisotropy of quartz and structural size, a pure TSh mode is impossible when QCR works, in which other modes like flexural, and face-shear modes are usually coupled together. In order to suppress these unwanted modes, the length/thickness ratio of the quartz plate should be chosen properly [6-9]. During the structural design process, the frequency spectrum is usually used to analyze the mode coupling of QCRs [6], from which certain length/ thickness ratios that are related to strong mode coupling and must be excluded can be clearly achieved. Additionally, there are still some anharmonic overtones (also called spurious modes) whose resonance frequencies are extremely close to TSh operating mode [10]. Spurious modes can lead to response admittance, which is also unexpected and should be refrained as far as possible. For suppressing spurious modes, some methods are developed, such as the stepped bi-mesa structure of AT-cut quartz plate [11, 12], and lateral field excitation [13, 14].

Temperature is an important factor that should be considered during the structural design of QCRs. Material parameters like elastic constant, piezoelectric coefficient, and dielectric constants, are related to the ambient temperature. Meanwhile, unmatched thermal expansion coefficients between quartz and electrodes can lead to thermal stress, which can furthermore contribute to the QCR's working performance. In order to qualitatively reveal the underlying mechanism and quantitatively obtain the frequency shift caused by thermal variation, many efforts have been carried out during the past decades [15-19]. In 1979, an incremental field theory was proposed by Tiersten [15], based on which the frequency temperature characteristics of the operating TSh mode in an infinite quartz plate were revealed. After that, by expanding the incremental displacement into different series forms along the thickness direction, the frequency-temperature relationship of QCRs was obtained by Lee and Yong [16, 17], Yang [18], and Wang [19]. It is expected that a QCR with good temperature stability can be achieved via some methods, such as novel structure design [20], additional compensating circuits [21], attached compensation layer with opposite thermal expansion coefficients [22], and so forth.

However, the works mentioned above are for ideal QCRs without any fabrication error. Actually, the error is not inevitable during the manufacturing process, *e.g.*, the parallelism error that is usually encountered when cutting the quartz plate from crystal columns, which can destroy the symmetry and then

furthermore affect the working performance. Manufacturing error usually has a great influence on the transmission characteristics and resonant frequency of resonators, which should be reduced to the minimum [23, 24]. For example, it has been revealed that the angular error caused by loss of parallelism has a great effect on the impedance, inductance, Q factor, and spurious modes [25]. In addition, the capacitance, sensitivity, electrostatic spring constant, and reliable operation range of accelerometers also vary as the oblique angle of the electrode-plate changes [26, 27]. To the knowledge of authors, the influence of parallelism error on performance indices of QCRs including resonant frequency, mode shape, and admittance has not been revealed so far, which is just the origin of the present contribution.

In this paper, the coupled vibration analysis of QCRs with an inclined crystal plate is carried out, and the influence mechanism of parallelism error is revealed from the perspectives of theoretical analysis and numerical simulations. Firstly, the framework of three-dimensional (3D) thermal incremental field equations is introduced in Part 2, which degrades into two-dimensional (2D) equations when straight-crested waves are considered for a finite QCR in Section 3. With the aid of the COMSOL Multiphysics software, the free vibration and forced vibration are analyzed and the influence of parallelism error is emphasized in Section 4. Finally, some conclusions are drawn. The conclusions obtained and methodologies adopted in this paper can provide a basic understanding of coupled vibrations of QCRs with parallelism error, which are also of significance for other acoustic devices.

2. The 3D thermal incremental field equations

For investigating the non-parallelism effect when external temperature varies, the 3D thermal incremental field equations are utilized in this paper, which are summarized in this section. Firstly, the equations of motion and electrostatics in the thermal increment field are [28]

$$
\begin{aligned}
\beta_{ik}\sigma_{kj,j} &= \rho u_{i,tt}, \\
D_{i,i} &= 0,
\end{aligned}
\tag{1}
$$

where σ_{ij} and D_i (i, j, k=1,2,3) represent the incremental stress and the incremental electric displacement, respectively. ρ is the mass density, $\boldsymbol{u}$ denotes the incremental displacement vector, and t denotes the time. An index after a comma denotes partial differentiation with respect to the coordinate or time. For piezoelectric media, the constitutive equations are

3

$$\sigma_{ij} = D_{ijkl}s_{kl} - e_{kij}^{\Theta}E_k,$$
$$D_i = e_{kij}^{\Theta}s_{jk} + \varepsilon_{ik}^{\Theta}E_k, \tag{2}$$

with s_{kl} and E_k representing the strain and electric field in the piezoelectric incremental field, which are controlled by

$$s_{ij} = \frac{1}{2}(\beta_{kj}u_{k,i} + \beta_{ki}u_{k,j}),$$
$$E_i = -\varphi_{,i}. \tag{3}$$

Here φ is the incremental potential. In Eqs. (1), (2) and (3), the elastic constant D_{ijkl}, piezoelectric coefficient e_{kij}^{Θ}, dielectric constant $\varepsilon_{ik}^{\Theta}$, and thermal expansion coefficient β_{ik} in the thermal incremental field are expressed as

$$D_{ijkl} = C_{ijkl} + D_{ijkl}^{(1)}\Theta + D_{ijkl}^{(2)}\Theta^2 + D_{ijkl}^{(3)}\Theta^3,$$
$$e_{ijk}^{\Theta} = e_{ijk} + e_{ijk}^{(1)}\Theta + e_{ijk}^{(2)}\Theta^2 + e_{ijk}^{(3)}\Theta^3,$$
$$\varepsilon_{ik}^{\Theta} = \varepsilon_{ik} + \varepsilon_{ik}^{(1)}\Theta + \varepsilon_{ik}^{(2)}\Theta^2 + \varepsilon_{ik}^{(3)}\Theta^3,$$
$$\beta_{ik} = \delta_{ik} + \alpha_{ik}^{(1)}\Theta + \alpha_{ik}^{(2)}\Theta^2 + \alpha_{ik}^{(3)}\Theta^3, \tag{4}$$

with $\Theta = \Delta T = (T-T_0)$ being the temperature change from a reference temperature T_0 set as 25°C. C_{ijkl}, e_{ijk}, ε_{ik} are the corresponding values measured at constant electric field and temperature, respectively. $D_{ijkl}^{(n)}$, $e_{ijk}^{(n)}$ and $\varepsilon_{ik}^{(n)}$ ($n = 1,2,3$) are the nth-order thermoelastic constants, nth-order temperature derivative of the piezoelectric constants, and nth-order temperature coefficients of the dielectric permittivity constants, respectively. β_{ik} is a non-dimensional parameter, δ_{ik} represents the Kronecker delta, and $\alpha_{ik}^{(n)}$ is the nth-order thermal expansion coefficient of quartz. In the following section, the coupled vibration of QCRs will be discussed with the aid of Eqs. (1) - (4) motioned above.

3. Theoretical analysis of QCRs

In this paper, a QCR consisting of an AT-cut quartz plate and two partial electrodes is considered, such as Fig. 1, with their thickness values respectively denoted by h_q, h_e^1 and h_e^2. Because of inevitable fabrication errors, the plate surface is not standard with a parallelism error, which is described by θ in Fig. 1. Therefore, the parallelism error can be calculated via $\Delta h_q = \tan(\theta) \cdot l_q / 2$, in which Δh_q stands for the thickness

4

variation related to a flat surface. Generally, parallelism error can be detected by several methods, such as stylus measurement, horizontal datum measurement [29], and interferometry [30]. For investigating the non-parallelism effect when external temperature varies, a 2D model with the thickness direction denoted by x_2 is considered, which can depict the straight-crested waves propagating in the x_1 direction. Therefore, the vibration is independent of x_3, i.e., $\partial/\partial x_3 = 0$, and the 2D thermal incremental field equations are reduced as

$$
\begin{aligned}
&\beta_{11}\left(\sigma_{1,1}+\sigma_{6,2}\right)=\rho u_{1,tt}, \\
&\beta_{22}\left(\sigma_{6,1}+\sigma_{2,2}\right)+\beta_{23}\left(\sigma_{5,1}+\sigma_{4,2}\right)=\rho u_{2,tt}, \\
&\beta_{32}\left(\sigma_{6,1}+\sigma_{2,2}\right)+\beta_{33}\left(\sigma_{5,1}+\sigma_{4,2}\right)=\rho u_{3,tt}, \\
&D_{1,1}+D_{2,2}=0.
\end{aligned}
\tag{5}
$$

Here u_1 and u_2 stand for the displacements in the x_1 and x_2 directions, respectively. Here, the double indices i, j and k has been converted to a single index p or q (p, q=1,2…6) [31].
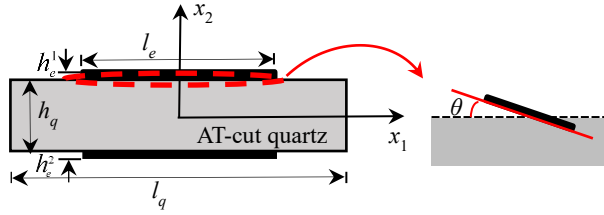
Fig. 1. Schematic of the QCR with a parallelism error on the top surface

Correspondingly, the constitutive equation (2) is expressed

$$
\begin{aligned}
&\sigma_1 = D_{11}s_1 + D_{12}s_2 + D_{14}s_4 - e_{11}^{\Theta}E_1, \\
&\sigma_2 = D_{21}s_1 + D_{22}s_2 + D_{24}s_4 - e_{12}^{\Theta}E_1, \\
&\sigma_4 = D_{41}s_1 + D_{42}s_2 + D_{44}s_4 - e_{14}^{\Theta}E_1, \\
&\sigma_5 = D_{55}s_5 + D_{56}s_6 - e_{25}^{\Theta}E_2, \\
&\sigma_6 = D_{65}s_5 + D_{66}s_6 - e_{26}^{\Theta}E_2, \\
&D_1 = e_{11}^{\Theta}s_1 + e_{12}^{\Theta}s_2 + e_{14}^{\Theta}s_4 + \varepsilon_{11}^{\Theta}E_1, \\
&D_2 = e_{25}^{\Theta}s_5 + e_{26}^{\Theta}s_6 + \varepsilon_{22}^{\Theta}E_2,
\end{aligned}
\tag{6}
$$

and Eq. (3) can be simplified as

$$
\begin{aligned}
&s_1 = \beta_{11}u_{1,1}, \quad s_2 = \beta_{22}u_{2,2} + \beta_{23}u_{3,2}, \quad s_3 = 0, \\
&s_4 = \beta_{23}u_{2,2} + \beta_{33}u_{3,2}, \quad s_5 = \beta_{23}u_{2,1} + \beta_{33}u_{3,1}, \\
&s_6 = \beta_{11}u_{1,2} + \beta_{23}u_{3,1} + \beta_{22}u_{2,1}, \\
&E_1 = -\varphi_{,1}, \quad E_2 = -\varphi_{,2}, \quad E_3 = 0.
\end{aligned}
\tag{7}
$$

Compared with the crystal plate, the electrodes are so thin, so that the elasticity can be neglected. Then, only considering the inertial effect is enough to calculate the resonance of QCRs [32-34]. Hence, the boundary condition on the upper and bottom surfaces are

$$\begin{cases} \sigma_6 = -\rho'h_e^1 u_{1,tt}, \ \sigma_2 = -\rho'h_e^1 u_{2,tt}, \quad \varphi = +(0.5V)\exp(i\omega t), \quad \text{at } x_2 = +0.5h_q, \ |x_1| \leq 0.5l_e \\ \sigma_6 = +\rho'h_e^2 u_{1,tt}, \ \sigma_2 = +\rho'h_e^2 u_{2,tt}, \quad \varphi = -(0.5V)\exp(i\omega t), \quad \text{at } x_2 = -0.5h_q, \ |x_1| \leq 0.5l_e \quad (8) \\ \sigma_6 = 0, \ \sigma_2 = 0, \ D_2 = 0, \quad \text{at } x_2 = \pm 0.5h_q, \ 0.5l_e \leq |x_1| \leq 0.5l_q \end{cases}$$

Here, V is the driving voltage, ω is the driving frequency, and ρ' denotes mass density of electrodes. At left and right edges $x_1 = \pm 0.5l_q$ of the quartz crystal plate,

$$\sigma_6 = \sigma_1 = 0, \ D_1 = 0. \quad (9)$$

Totally speaking, the vibration response of QCRs is solving the straight-crested waves governed by Eq. (5) under consideration of boundary conditions (8) and (9). Under the external voltage, the electric field E_2 can be calculated via

$$E_2 = -V\exp(i\omega t)/h_q. \quad (10)$$

After the electrical field D_2 is obtained, the total charges on the top electrode and the equivalent current of the AT-cut quartz plate are respectively [35]

$$Q = -2w_e \int_{-l_e}^{l_e} D_2 dx_1, \quad I = i\omega Q. \quad (11)$$

Then, the admittance of the QCR per unit electrode area can be expressed as [31]

$$Y = I/V/(4l_e w_e). \quad (12)$$

with l_e and w_e representing the length and width of the electrode, respectively.

4. Numerical results and discussions

As the numerical example, the AT-cut QCR ($\rho = 2.65 \times 10^3$ kg/m^3) covered by silver electrodes with mass density $\rho' = 10.49 \times 10^3$ kg/m^3 is considered. The material constants of the AT-cut crystal for the nth-order

temperature derivatives of the elastic constant, piezoelectric constant, and dielectric constant, as well as the thermal expansion coefficient, are obtained in Refs. [31, 36-38], which are listed in Appendix. The length and width of the crystal plate are respectively $l_q = 1.2$ mm and $h_q = 0.03$ mm, and the structural parameters of electrodes are $l_e = 0.7$ mm, $w_e = 0.4$ mm, $h_e^1 = 0.1\times10^{-3}$ mm and $h_e^2 = 0.2\times10^{-3}$ mm.

Eq. (5) is so complex that an exact theoretical solution is hardly achieved for the QCR with a parallelism error. For exactly analyzing the free vibration properties, a 2D model is established and solved in the coefficient-formed PDE module of the COMSOL Multiphysics software. The parameters are input using Eqs. (5), (6) and (7), and the boundary conditions are set according to Eqs. (8) and (9). The solving procedure is the same as traditional Finite Element Method (FEM) simulations. The external voltage is set as zero for free vibration analysis, and the electrodes are added via an additional mass layer. Mapped rectangular elements are adopted with at least twenty elements distributed along the plate thickness direction and recomputation has been carried out with smaller elements before the final simulation, which can make the numerical results convergent and accurate. The element size is controlled via the node numbers along the plate length. Larger node number indicates finer meshes, which will produce more accurate resonant frequency, such as the Table 1. Therefore, the plate length is distributed 15 nodes during the simulations. Not limited by free vibration, another module, *i.e.*, piezoelectric module, is adopted when $V = 3$ V, which is used to investigate the admittance of QCR and validate the results from the PDE module.

Table 1. The resonant frequency f_0 under different node numbers

Node number	6	7	8	9	10	11	12	13	14	15
f_0 (MHz)	53.222 2900	53.222 2900	53.222 2903	53.222 2907	53.222 2911	53.222 2914	53.222 2917	53.222 2920	53.222 2922	53.222 2923

4.1. The working performance of QCRs when the top surface is inclined

As an important performance index of QCR, the resonant frequency plays an important role in service. At resonances, the electrical output is maximal. Before fabrication, frequency spectrum, *i.e.*, the quantitative relation between resonant frequency and length/thickness ratio l_q/h_q, is usually examined for structural design, as shown in Fig. 2. Curves consisting of different data points correspond to different modes. Totally speaking, curves are classified into two families, *i.e.*, the relatively horizontal curves and the oblique ones.

Taking the ideal QCR without non-parallelism, *i.e.*, $\theta = 0°$, for example. The flat one with the resonant frequency near 53.2 MHz represents the essentially thickness-shear mode, which is the anticipated first-order thickness-shear (TSh1) mode. The other flat portions represent the spurious modes. The oblique curves, represent face-shear (FS) modes, extensional (E) modes or flexural (F) modes, and the interaction between TSh1 modes and FS, E or F modes indicates mode coupling. It can be seen from Fig. 2a that the parallelism parameter θ has a great impact on the frequency spectrum, and a larger non-parallelism will lead to a lower resonant frequency. It is because the resonant frequency is dependent on the reciprocal of plate thickness, and the increment of θ leads to a thicker crystal plate.

(a)

(b)
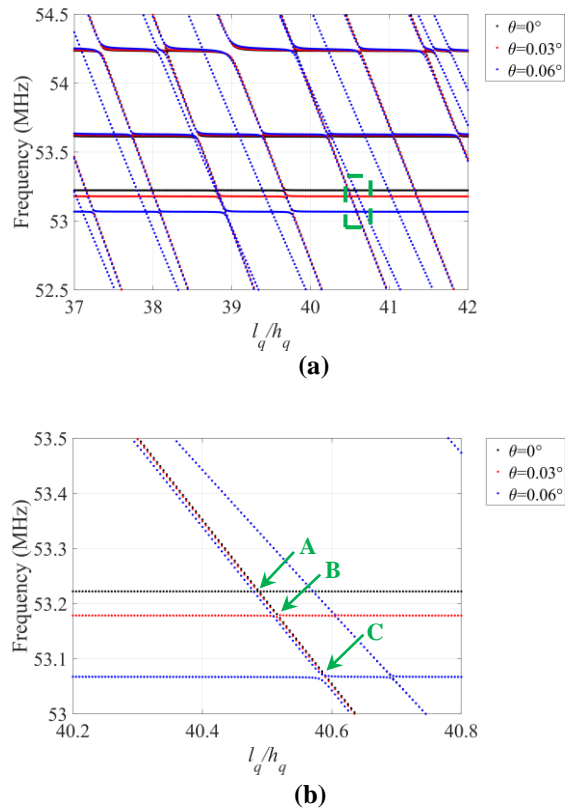
Fig. 2. (**a**) Frequency spectra under different parallelism error; (**b**) Magnification of green rectangular area in Fig. 2(**a**)

As we known, strong mode coupling is easy to occur at the beginning or ending points of the flat portions [39, 40]. Obviously, the non-parallelism has changed the intersection regions. To clearly demonstrate the influence of non-parallelism on mode coupling, Fig. 3a, 3b and 3c respectively illustrate the magnified frequency spectra near the mode coupling position when θ is 0, 0.03°and 0.06°. Obviously, the flat TSh1 mode (black line) intersects with the E mode (green line), which means the two modes are not coupled and can be decoupled easily [41]. However, when θ is chosen as 0.03° or 0.06°, a strong mode

coupling phenomenon appears, as shown in Fig. 3b and 3c. Because of the inclined surface, the QCR is not symmetric about $x_1 = 0$, and the TSh1 mode is difficult to separate from other modes.

The frequency-temperature curve, quantitatively depicting the frequency shift caused by external thermal variation, is usually utilized to analyze the stability of QCRs [42-44]. The influence of θ on the frequency-temperature curve is illustrated in Fig. 4. For the case of $\theta = 0°$, *i.e.*, the crystal plate is symmetric without parallelism error, the frequency tolerance of the TSh1 mode in QCRs is ±15ppm when the thermal variation locates [−75°C, 75°C], marked with the green dash line in Fig. 4a. Owing to the decoupling between the E mode and TSh1 mode, the frequency shift value detected in service totally belongs to the TSh1 branch. However, if θ is not zero, the frequency shift value detected does not totally belong to the TSh1 mode anymore. In some working temperature ranges, the E mode dominates, which makes the frequency shift increase rapidly. It is the activity dip [45], which should be avoided for QCR. Taking ±15ppm marked with the green dash line as the frequency tolerance, the anomaly temperature variation region corresponding to activity dip can be calculated via vertical red lines in Fig. 4b and 4c. It is [−16°C, 3°C] when θ is 0.06°, which is larger than that of $\theta = 0.03°$, *i.e.*, . [−2°C, 9°C]. In other words, a larger parallelism error will increase the probability of activity dip, which is harmful to QCRs.


(a)   (b)
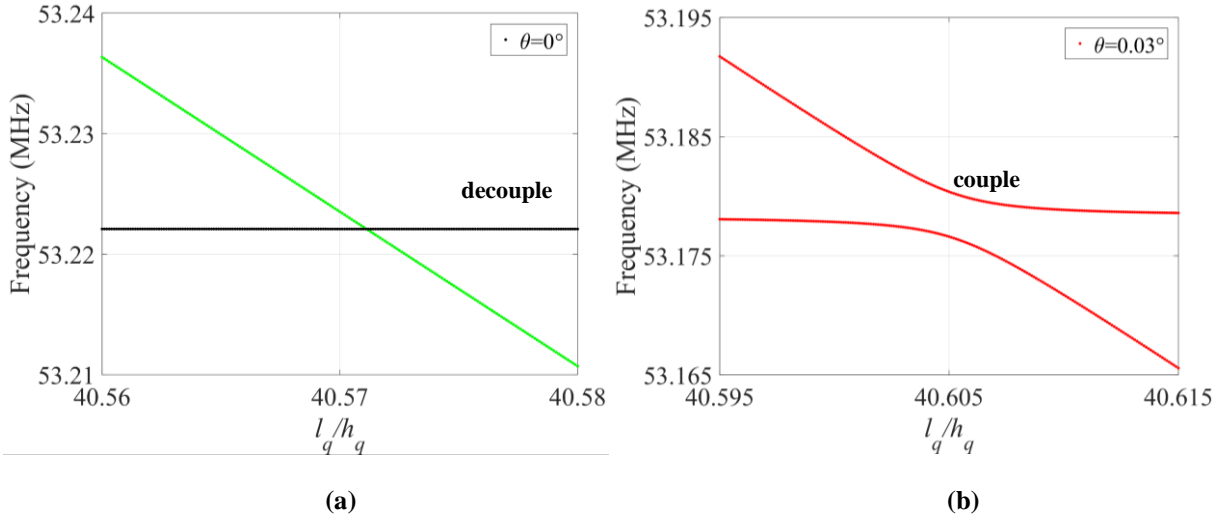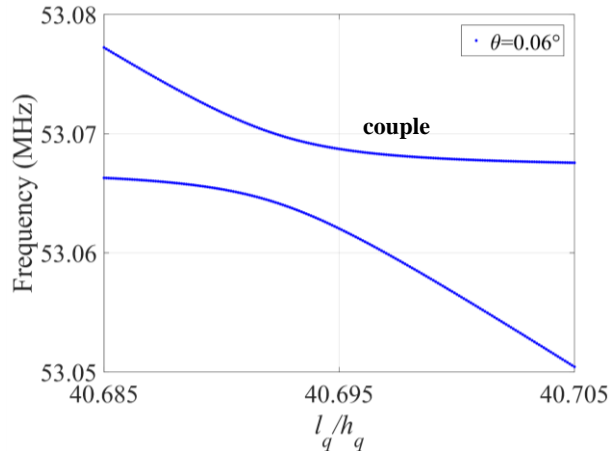
(c)

Fig. 3. The local frequency spectra under different parallelism errors: (**a**) Region A: θ=0°; (**b**) Region B: θ=0.03°; (**c**) Region C: θ=0.06°

In order to verify that strong mode coupling is the main reason for activity dip, Fig. 5 shows the mode shape represented by u_1 at three typical cases, *i.e.*, ΔT respectively equals −30°C, 0°C, and 73°C when θ = 0.03°. When $\Delta T = -30$°C, the frequency shift exceeds ±15ppm without activity dip. Combined with Fig. 6a, it can be found that mode coupling is weak. As ΔT increases, the activity dip occurs, such as $\Delta T = 0$°C in Fig. 4b. It is clearly seen from Fig. 5b that the mode coupling is strong. When $\Delta T = 73$°C, there is no mode coupling in Fig. 5c, and the activity dip disappears. Therefore, it is strong mode coupling that induces activity dip. Totally speaking, the parallelism error is not beneficial for QCRs, and should be suppressed as little as possible during fabrications.
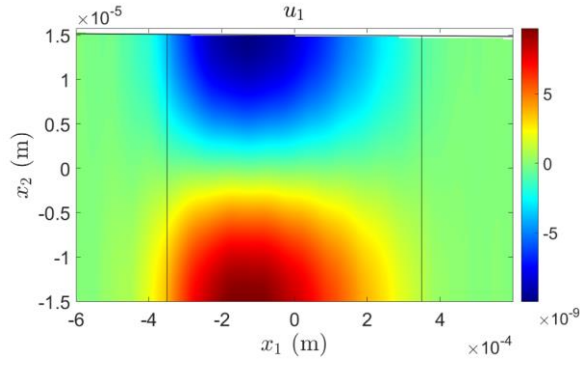

(a)

(b)

10
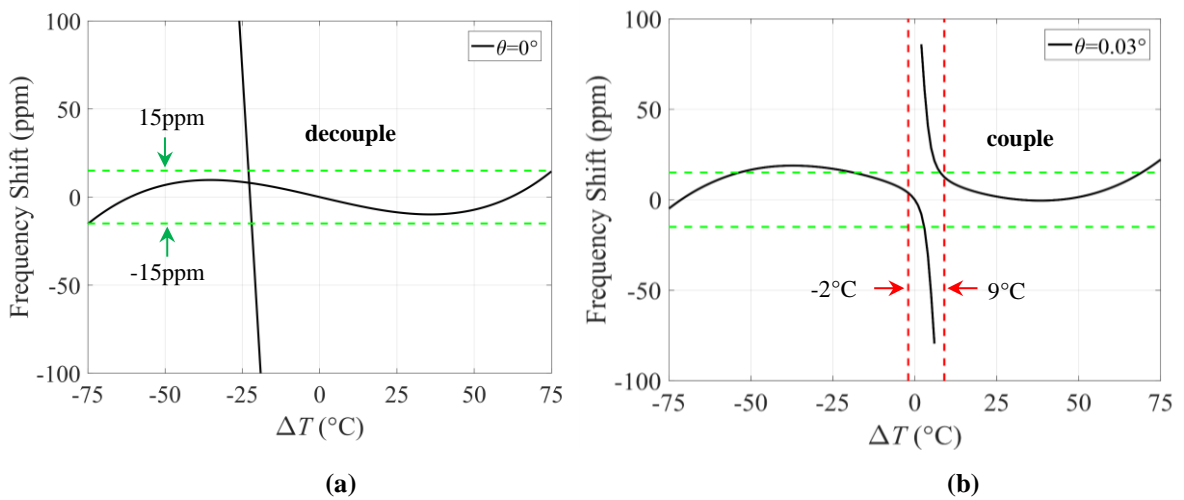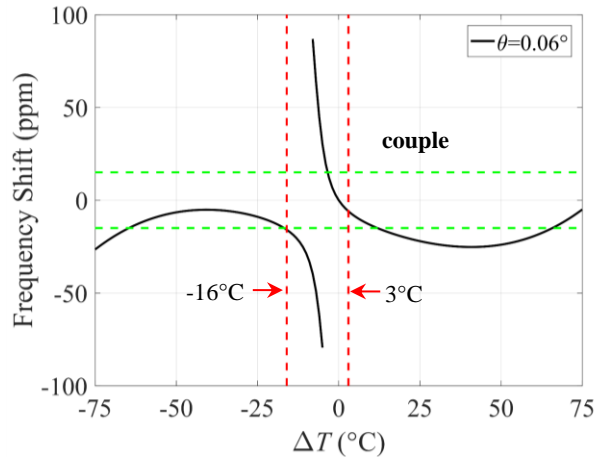
(c)

Fig. 4. The frequency-temperature curves when θ is (**a**)0°, (**b**) 0.03° and (**c**) 0.06°
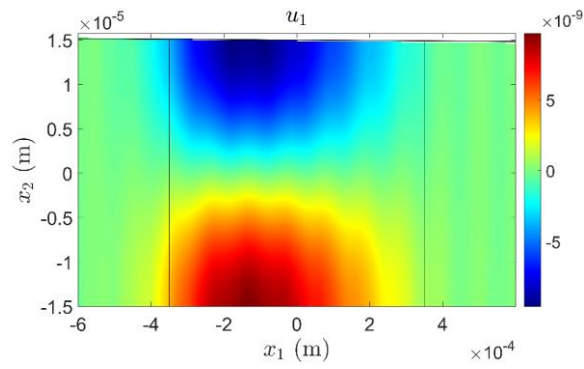
(a)
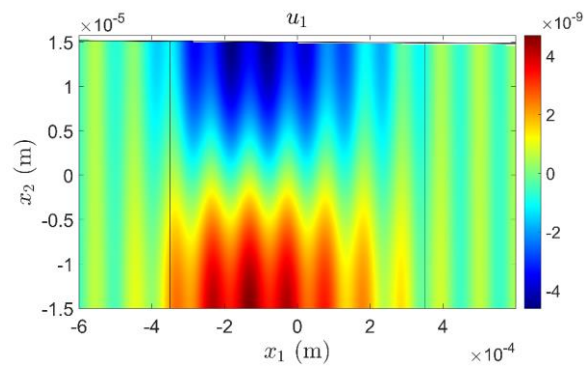
(b)

(c)

Fig. 5. Mode shapes when θ=0.03°: (**a**) $\Delta T = -30$°C; (**b**) $\Delta T = 0$°C; (**c**) $\Delta T = 73$°C

For further investigating the influence of θ on the working performance of QCRs, the force vibration is analyzed when $l_q/h_q = 40$, and the admittance and phase distributions are demonstrated in Fig. 6. The absolute value of admittance reaches its maxima at three different resonant frequencies, *i.e*., 53.22MHz for $\theta = 0$°, 53.17MHz for $\theta = 0.03$° and 53.06MHz for $\theta = 0.06$°. They are consistent with the frequencies of TSh1 shown in Fig. 2, which can validate the correctness of the numerical results in this paper. Additionally, it can be seen that the resonant frequency of TSh mode decreases as θ increases, which also coincides with the results obtained from free vibration analysis in Fig. 2. It should be noted that different from 0.03° and 0.06°, there is no obvious electrical and phase response at the second peak value when $\theta = 0$°. This mode is antisymmetric about $x_1 = 0$, and the whole QCR is strictly symmetric with $x_1 = 0$, then the positive and negative charges generated by the piezoelectric effect completely vanish. However, for QCRs with a parallelism error, the crystal plate is not symmetric along the thickness direction anymore, and mode coupling causes electrical responses.
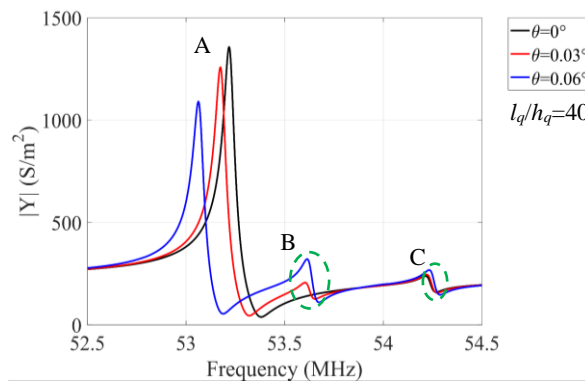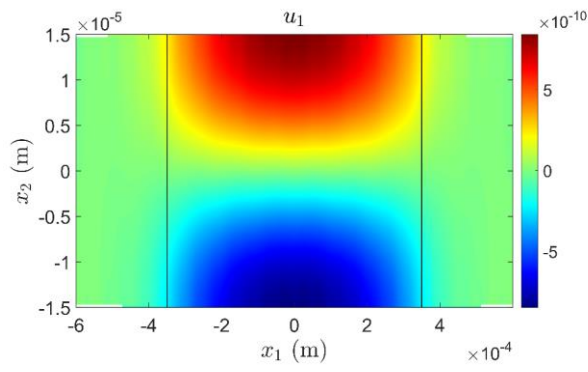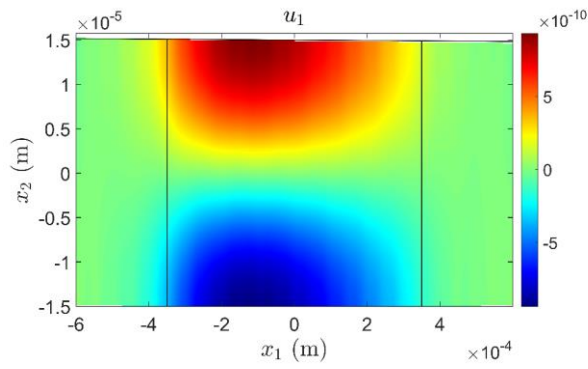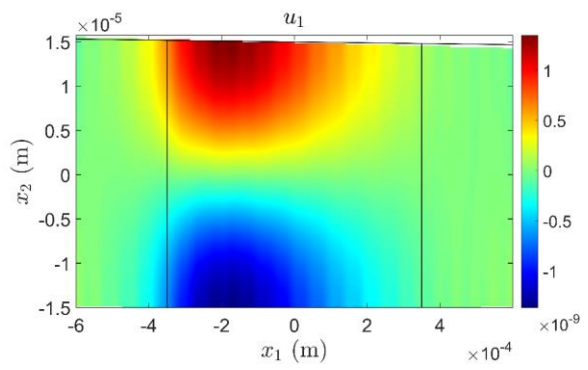

(a)
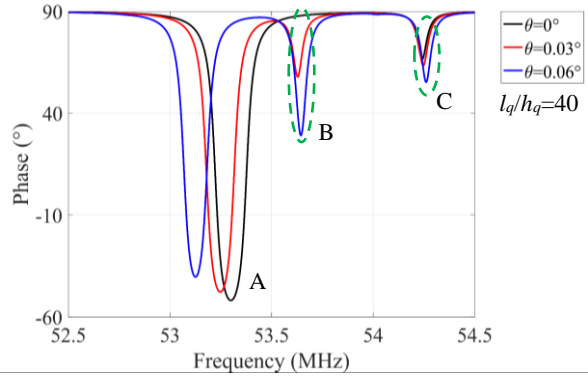
(b)

Fig. 6. The (**a**) admittance and (**b**) phase responses

(a)

(b)

(c)

Fig. 7. The u_1 distribution near the first peak value: (**a**) $\theta = 0°$; (**b**) $\theta = 0.03°$; (**c**) $\theta = 0.06°$

It also can be seen from Fig. 6a that the maximal value at the first resonance decreases with the increase of θ. For interpreting this phenomenon, the u_1 distribution is plotted and shown in Fig. 7. For a perfect plate without parallelism error, the vibration energy is captured in the electroded region because of energy trapping, as shown in Fig. 7a. However, for QCRs with a parallelism error, the vibration deviates towards the left, *i.e.*, the plate region with a larger thickness, and vibration begin to leak out of electrodes as θ increases. It is because the crystal plate is not symmetric when θ is not zero. The plate region with a larger thickness processes a lower cut-off frequency, which makes the TSh1 wave attenuate slowly. Therefore, it is the vibration leaking caused by the parallelism error that reduces the electrical response at the second resonance.

4.2. The working performance when both surfaces of QCRs are inclined

After analyzing the working performance of QCRs with the top surface inclined, the circumstance corresponding to both surfaces inclined is also considered in this paper. For convenience, it is assumed that parallelism errors on the top and bottom surfaces are the same, and both of them incline in the same or opposite direction, as shown in Fig. 8.
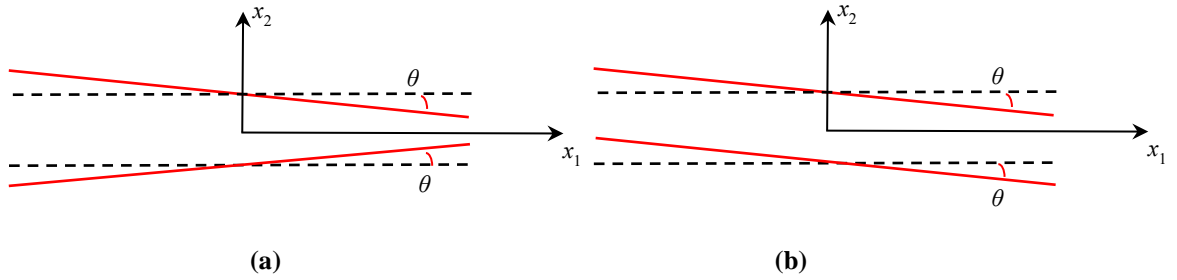

(a)   **(b)**

Fig. 8. QCRs with both surfaces inclined in the (**a**) opposite direction and (**b**) the same direction

Both the free vibration and forced vibration are analyzed. Taking the QCRs with both surfaces inclined in the opposite direction, for example, Fig. 9a and 9b respectively depict the frequency spectra and the admittance response. Obviously, the variations of resonant frequency and admittance in Fig. 9 are significantly larger than that with one single inclined surface. The resonant frequency in Fig. 9a decreases with the increasing θ, which agrees with Fig. 2a. From the admittance response in Fig. 9b that is corresponding to the $l_q/h_q = 40$ labeled with green dash lines in Fig. 9a, it can be seen that there is an irregular ripple near the TSh1 mode when $\theta = 0.06°$, which is because of strong coupling induced by the asymmetry along the plate thickness.

For the QCR with both surfaces inclined in the same direction, Fig. 10 shows the frequency spectra and the admittance response when $l_q/h_q = 40$. By contrast, the parallelism errors on this condition have a tiny effect on the working performance of QCRs. As we know, the resonant frequency mainly depends on the plate thickness. When the top and bottom surfaces incline synchronously, the plate thickness hardly changes, and then the resonant frequency hardly varies. Therefore, it is anticipated that fabricating the same parallelism error in another plate surface is an efficient method to keep the previous working performance of QCRs.
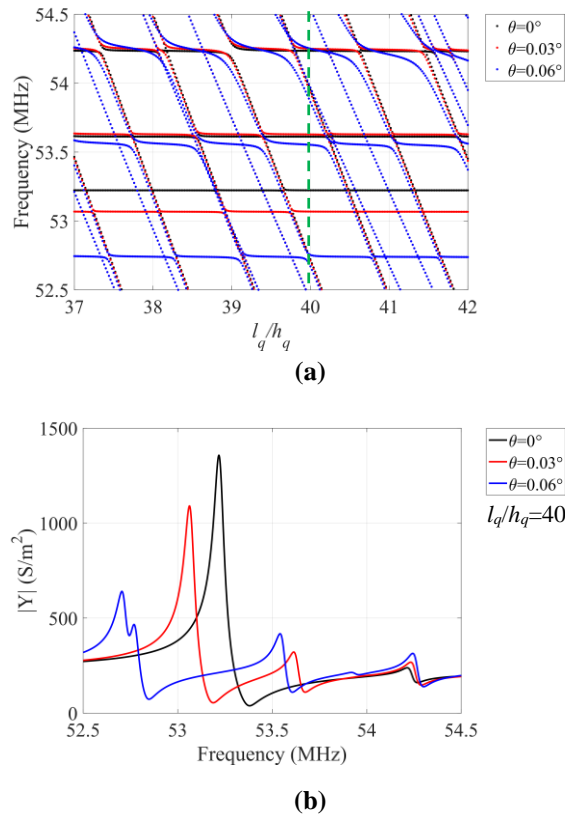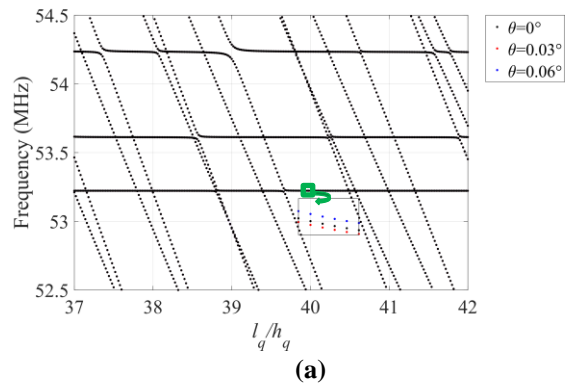

(a)

(b)

Fig. 9. The (**a**) frequency spectra and (**b**) admittance response of QCR with both surfaces inclined in the opposite direction
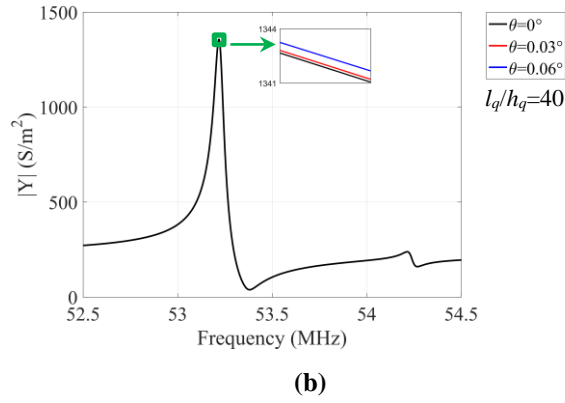

(a)

15

(b)

Fig. 10. The (**a**) frequency spectra and (**b**) admittance response of QCR with both surfaces inclined in the same direction

5. Conclusions

The influence of the non-parallelism effect on the free vibration and forced vibration is systematically investigated with the aid of COMSOL Multiphysics software. Totally speaking, the non-parallelism effect is not beneficial for the performance improvement of QCRs. The resonant frequency, as well as admittance at resonance, has been reduced in a QCR with its one or two surfaces inclined. Additionally, the non-symmetricity caused by the non-parallelism effect makes mode coupling easier to occur, which increases the probability of activity dip and is harmful to QCR's thermal stability. The quantitative results and qualitative conclusions obtained in this paper provide guidance for the structural design of QCRs and other similar devices.

Author's Contribution

LMJ, LN and LP constructed the model and carried out the theoretical analyses and numerical simulations. LDZ and KIE conducted the investigations and provided research ideas. QZH summarized the results and determined the research direction. QZH, KIE, and MTF provided the funding and support. All authors discussed the results and wrote the manuscript.

Availability of Data and Materials

The data used and analyzed in this study are available from the corresponding author upon reasonable request.

Declarations

Conflict of interest The authors declare no potential conflicts of interest with respect to the research, authorship, and/or publication of this article.

Ethical Approval and Consent to Participate This article does not address ethical issues. The authors confirm that they have no known competing financial interests or personal relationships that could have appeared to influence the work reported in this paper.

References

[1] Shockley W, Curran DR, Koneval DJ. Trapped-energy modes in quartz filter crystals. J Acoust Soc Am. 1967;41(4B):981-993.

[2] Tiersten HF. Analysis of overtone modes in monolithic crystal filters. J Acoust Soc Am. 1977;62(6):1424-1430.

[3] He HJ, Liu JX, Yang JS. Analysis of a monolithic crystal plate acoustic wave filter. Ultrason. 2011;51(8):991-996.

[4] Xie JM, Hu YT. A two-dimensional model on the coupling thickness-shear vibrations of a quartz crystal resonator loaded by an array spherical-cap viscoelastic material units. Ultrason. 2016;71(2):194-198.

[5] Zhao ZN, Qian ZH, Wang B. Thickness-shear vibration of a Z-strip AT-cut quartz crystal plate with nonuniform electrode pairs. Ferroelectr. 2017;506(1):48-62.

[6] Mindlin RD. Thickness-shear and flexural vibrations of crystal plates. J Appl Phys. 2008;22(3):316-323.

[7] Wang JN, Hu YT, Yang JS. Frequency spectra of AT-cut quartz plates with electrodes of unequal thickness. IEEE Trans Ultrason Ferroelectr Freq Control. 2010;57(5):1146-51.

[8] Chen GJ, Wu RX, Wang J, Du JK, Yang JS. Five-mode frequency spectra of x3-dependent modes in AT-cut quartz resonators. IEEE Trans Ultrason Ferroelectr Freq Control. 2012;59(4):811-816.

[9] Li N, Wang B, Qian ZH. Coupling vibration analysis of trapped-energy rectangular quartz resonators by variational formulation of Mindlin's theory. Sensors. 2018;18(4):986.

[10] Mindlin RD, Spencer WJ. Anharmonic, thickness-twist overtones of thickness-shear and flexural vibrations of rectangular, AT-cut quartz plates. J Acoust Soc Am. 1967;42(6):1268-1277.

[11] Goka S, Ishizaki A, Sekimoto H, Watanabe Y. Effect of stepped bi-mesa structures on spurious vibrations of AT-cut quartz plates. Jpn J Appl Phys. 2000;39(5B):3054-3055.

[12] Goka S, Tamura T, Sekimoto H, Watanabe Y, Sato T, Sato K. Mode decoupling effect of multistepped bi-mesa AT-cut quartz resonators. Jpn J Appl Phys. 2004;43(5B): 3016-3019.

[13] Ma TF, Wang J, Du JK, Yang JS. Resonances and energy trapping in AT-cut quartz resonators operating with fast shear modes driven by lateral electric fields produced by surface electrodes. Ultrason. 2015; 59:14-20.

[14] Zaitsev BD, Shikhabudinov AM, Borodina IA, Teplykh AA, Kuznetsova IE. Composite lateral electric field excited piezoelectric resonator. Ultrason. 2017; 73:125-129.

[15] Tiersten HF. Temperature dependence of the resonant frequency of electroded doubly-rotated quartz thickness-mode resonators. J Appl Phys. 1979;50(12):8038-8051.

[16] Lee PCY, Yong YK. Frequency-temperature behavior of thickness vibrations of doubly rotated quartz plates affected by plate dimensions and orientations. J Appl Phys. 1986;60(7):2327-2342.

[17] Lee PCY, Yong YK. Temperature derivatives of elastic stiffness derived from the frequency-temperature behavior of quartz plates. J Appl Phys. 1984;56(5):1514-1521.

[18] Yang JS. Equations for small fields superposed on finite biasing fields in a thermoelectroelastic body. IEEE Trans Ultrason Ferroelectr Freq Control. 2003;50(2): 187-192.

[19] Wang J. The frequency-temperature analysis equations of piezoelectric plates with Lee plate theory. IEEE Trans Ultrason Ferroelectr Freq. Control. 1999; (46)4:1042-1046.

[20] Yong YK, Vig J, Ballato A, Kubena R, M'Closkey R. Frequency-temperature analysis of MEMS AT-cut quartz resonators. in Proc IEEE Int Freq Control Symp Tampa, FL, USA. 2003;1095-1099.

[21] Matko V. Multiple quartz crystals connected in parallel for high-resolution sensing of capacitance changes. Sensors. 2022;22(13):5030.

[22] Naumenko NF. Temperature behavior of SAW resonators based on LiNbO₃/quartz and LiTaO₃/quartz substrates. IEEE Trans Ultrason Ferroelectr Freq Control. 2021;68(11):3430-3437.

[23] Wang YH, Qin ZK, Wang CX. Effects of manufacturing errors on the characteristics of a polymer vertical coupling microring resonator. J Semicond. 2012;33(10): 104007.

[24] Huang JY, Zhao Y, Xia GM, Shi Q, Qiu AP. Accurate identification of the evolution of MEMS resonant accelerometer residual stresses at the wafer-die-chip level. J Microelectromech S. 2022;31(4): 524-532

[25] Pentovelis G, Boudy C, Jeannerot V. Influence of wafer symmetry on the dynamic parameters of rectangular plates. in Proc IEEE Int Freq Control Symp. 1999;453-456.

[26] Tay FEH, Xu J, Liang LC, Logeeswaran VJ, Yao YF. The effects of non-parallel plates in a differential capacitive microaccelerometer. J Micromech Microeng. 1999;9(4):283-293.

[27] Dong LX, Che LF, Sun LG, Wang YL. Effects of non-parallel combs on reliable operation conditions of capacitive inertial sensor for step and shock signals. Sensor Actuat A-Phys. 2005;121(2):395-404.

[28] Yong YK, Wei W. Lagrangian temperature coefficients of the piezoelectric stress constants and dielectric permittivity of quartz. in Proc IEEE Int Freq Control Symp. 2000; 364-372.

[29] Zhang J, Cai L. Interferometric straightness measurement system using triangular prisms. Opt Eng. 1998;37(6):1785-1789.

[30] Vannoni M, Molesini G. Paired interferometric measurement of planarity and parallelism. in Proc Opt Meas Syst. 2003;864-871.

[31] Tiersten HF. Linear Piezoelectric Plate Vibrations. New York: Plenum Press; 1969.

[32] Kosinski JA. Thickness vibrations of flat piezoelectric plates with massy electrodes of unequal thickness. IEEE Ultrasonics Symp. 2005;1(1):70-73.

[33] Liu N, Yang JS, Chen WQ. Effects of a mass layer with gradually varying thickness on a quartz crystal microbalance. IEEE Sensors J. 2011;11(8):1635-1639.

[34] Gu CL, Li P, Jin F, Chen GF, Ma LS. Effects of the imperfect interface and viscoelastic loading on vibration characteristics of a quartz crystal microbalance. Acta Mechanica. 2018;229(7):2967-2977.

[35] Yang JS. The Mechanics of Piezoelectric Structures.World Scientific; 2006.

[36] Bechmann R, Ballato AD, Lukaszek TJ. Frequency-temperature behavior of thickness modes of double-rotated quartz plates. in Proc IEEE Symp Freq Control. 1961;22-48.

[37] Bechmann R, Ballato AD, Lukaszek TJ. Frequency-temperature characteristics of quartz resonators derived from the temperature behavior of the elastic constants. in Proc IEEE Symp Freq Control. 1962;77-109.

[38] Yong YK, Wei W. Lagrangean versus classical formulation of frequency-temperature problems in quartz resonators. in Proc IEEE Int Freq Control Symp. 2001;828-837.

[39] Li N, Qian ZH, Wang B. Forced coupling vibration analysis of FBAR based on two-dimensional equations associated with state-vector approach. AIP Adv. 2018;8(9): 095306.

[40] Li N, Wang B, Qian ZH. Effects of mode couplings on the vibration characteristics of partially electroded thin-film bulk acoustic wave resonators. AIP Adv. 2019;9(6): 065203.

[41] He HJ, Yang JS, Zhang WP, Wang J. Effects of mode coupling on the admittance of an AT-cut quartz thickness-shear resonator. Chin Phys B. 2013;22(4):476-481.

[42] Yang JS, Zhang X. Vibrations of a crystal plate under a thermal bias. J Therm Stresses. 2003;26(5):467-477.

[43] Yong YK, Patel M, Tanaka M. Effects of thermal stresses on the frequency-temperature behavior of piezoelectric resonators. J Therm Stresses. 2007;30(6):639-661.

[44] Shen Q, Yang J, Xie JB, Ren S, Yuan WZ. An enhanced high-sensitivity micro resonant thermometer with axial strain amplification effect. in Proc IEEE Int Nano Conf. 2018;23-24.

[45] Ballato A; Tilton R. Electronic activity dip measurement. IEEE Trans Instrum Meas. 1978;27(1):59-65.

Appendix: Material parameters of AT-cut quartz.

The AT-cut quartz can be obtained by rotating the Y-cut quartz counterclockwise φ=35.25° around the x-axis, and then its elastic constant, piezoelectric constant, and dielectric constant can be obtained by Y-cut quartz through the Bond transformation matrix M.

$$M = \begin{bmatrix} 1 & 0 & 0 & 0 & 0 & 0 \\ 0 & \cos\varphi^2 & \sin\varphi^2 & \sin 2\varphi & 0 & 0 \\ 0 & \sin\varphi^2 & \cos\varphi^2 & -\sin 2\varphi & 0 & 0 \\ 0 & -0.5\sin 2\varphi & 0.5\sin 2\varphi & \cos 2\varphi & 0 & 0 \\ 0 & 0 & 0 & 0 & \cos\varphi & -\sin\varphi \\ 0 & 0 & 0 & 0 & \sin\varphi & \cos\varphi \end{bmatrix}. \tag{13}$$

The elastic constant matrix of Y-cut quartz crystal is

$$c' = \begin{bmatrix} c'_{11} & c'_{12} & c'_{13} & c'_{14} & 0 & 0 \\ c'_{12} & c'_{11} & c'_{13} & -c'_{14} & 0 & 0 \\ c'_{13} & c'_{13} & c'_{33} & 0 & 0 & 0 \\ c'_{14} & -c'_{14} & 0 & c'_{44} & 0 & 0 \\ 0 & 0 & 0 & 0 & c'_{44} & c'_{14} \\ 0 & 0 & 0 & 0 & c'_{14} & c'_{66} \end{bmatrix} \tag{14}$$

with $c'_{66} = (c'_{11} - c'_{12})/2$. There are six independent elastic constants in Y-cut quartz crystal, *i.e.*,

$$\begin{aligned} c'_{11} &= 86.74\text{GPa}, \quad c'_{12} = 6.99\text{GPa}, \quad c'_{33} = 107.2\text{GPa}, \\ c'_{13} &= 11.91\text{GPa}, \quad c'_{44} = 57.94\text{GPa}, \quad c'_{14} = -17.91\text{GPa}. \end{aligned} \tag{15}$$

Similarly, the piezoelectric constant matrix of Y-cut quartz crystal is

$$e' = \begin{pmatrix} e'_{11} & -e'_{11} & 0 & e'_{14} & 0 & 0 \\ 0 & 0 & 0 & 0 & -e'_{14} & -e'_{11} \\ 0 & 0 & 0 & 0 & 0 & 0 \end{pmatrix}, \tag{16}$$

with two independent piezoelectric constants e'_{11}=0.171C/m² and e'_{14}=-0.0406C/m². Similarly, the dielectric constant matrix of Y-cut quartz is

$$\varepsilon' = \begin{pmatrix} \varepsilon'_{11} & 0 & 0 \\ 0 & \varepsilon'_{11} & 0 \\ 0 & 0 & \varepsilon'_{33} \end{pmatrix}, \tag{17}$$

with two independent components ε'_{11}=39.21×10⁻¹²C/V/m and ε'_{33}=41.03×10⁻¹²C//V/m.

The elastic constants, piezoelectric constants, and dielectric constants of AT-cut quartz crystal plates are calculated as follows

$$\begin{aligned} c &= Mc'M^{\text{T}}, \\ e &= ae'M^{\text{T}}, \\ \varepsilon^{\text{T}} &= a\varepsilon'^{\text{T}}a^{\text{T}}. \end{aligned} \tag{18}$$

Here, coordinate transformation matrix a is

$$a = \begin{bmatrix} 1 & 0 & 0 \\ 0 & \cos\varphi & \sin\varphi \\ 0 & -\sin\varphi & \cos\varphi \end{bmatrix}. \tag{19}$$

Table A1 The nth-order temperature derivative of elastic constants of Y-cut quartz at 25 °C (n=1,2,3)

pq	$D_{(1)pq}(\times10^7\text{N/m}^2\text{/K})$	$D_{(2)pq}(\times10^4\text{ N/m}^2\text{/K}^2)$	$D_{(3)pq}(\times10\text{ N/m}^2\text{/K}^3)$
66	0.638907	0.619477	-0.996383
11	-0.591490	-1.007325	-0.5191845
44	-1.085111	-1.596966	-0.227747
14	-0.154782	0.088914	1.470771
13	-0.835112	-1.217100	-0.114015
33	-2.102364	-1.694237	0.887281

Table A2 The nth-order temperature derivative of piezoelectric constants of Y-cut quartz at 25 °C

(n=1,2,3)

pq	$e_{(1)pq}(\times10^{-6}\text{C/m}^2\text{/K})$	$e_{(2)pq}(\times10^{-9}\text{C/m}^2\text{/K}^2)$	$e_{(3)pq}(\times10^{-12}\text{C/m}^2\text{/K}^3)$
11	-1.37002	-0.748887	1.955179
14	3.12403	2.600050	-4.692380

Table A3 The nth-order temperature derivative of dielectric constants of Y-cut quartz at 25 °C (n=1,2,3)

pq	$\varepsilon_{(1)pq}(\times10^{-15}\text{C/V/m/K})$	$\varepsilon_{(2)pq}(\times10^{-18}\text{C/V/m/K}^2)$	$\varepsilon_{(3)pq}(\times10\text{C/V/m/K}^3)$
11	1.59020	5.377230	5.105736
33	5.46123	0.1894809	-9.230945

Table A4 First three orders thermal expansion coefficients of Y-cut quartz at 25 °C

pq	$\alpha_{(1)pq}(\times10^{-6}\text{/°C})$	$\alpha_{(2)pq}(\times10^{-9}\text{/°C})$	$\alpha_{(3)pq}(\times10^{-12}\text{/°C})$
11	13.71	6.5	-1.9
22	13.71	6.5	-1.9
33	7.48	2.9	-1.5